Available online at www.sciencedirect.com

ScienceDirect

Electrochimica Acta 52 (2007) 2166–2174

ELECTROCHIMICA Acta

www.elsevier.com/locate/electacta

Electrocatalysis by design: Effect of the loading level of Au nanoparticles–MnOx nanoparticles binary catalysts on the electrochemical reduction of molecular oxygen

Mohamed S. El-Deab [1,2], Takeo Ohsaka [*,1]

Department of Electronic Chemistry, Interdisciplinary Graduate School of Science and Engineering,
Tokyo Institute of Technology, 4259 Nagatsuta, Midori-ku, Yokohama 226-8502, Japan

Received 27 July 2006; received in revised form 19 August 2006; accepted 19 August 2006
Available online 20 September 2006

Abstract

This study concerns the efficient electrochemical reduction of molecular oxygen (O_2), in O_2-saturated 0.1 M KOH solution, to OH^- through a four-electron reduction pathway by a novel binary catalyst that is comprised of two kinds of catalysts, i.e., Au nanoparticles (nano-Au) and manganese oxide nanoparticles (nano-MnOx) electrodeposited onto a relatively inert substrate, e.g., glassy carbon (GC) electrode. The nano-Au catalyst is efficiently used for the electro-reduction of O_2 to hydrogen peroxide through a two-electron reduction pathway at a reasonably low overpotential. While the latter (i.e., nano-MnOx) is effectively used for the subsequent catalytic decomposition of the electrogenerated hydrogen peroxide to water and molecular oxygen. The dependence of the electrocatalytic activity of the proposed binary catalysts towards the oxygen reduction on the loading level of both species has been investigated in this paper. This is done aiming at the preparation of a binary catalyst composed of the optimum amounts of both species which supports an apparent four-electron reduction of O_2 at sufficiently low overpotential in replacement of the costly Pt-based electrocatalysts.

Keywords: Electrocatalysis; Nanoparticles; Metal air battery; Fuel cells; Catalytic disproportionation; Hydrogen peroxide

1. Introduction

The large overpotential associated with the oxygen reduction reaction (ORR) is one of the major challenges which call for the development of a high performance cathode catalyst [1–3]. The ORR is a reaction of indispensable importance in metal air batteries, fuel cells as well as in oxygen sensor [1,4–10]. So far, Pt and Pt-base alloys are superior to many other electrocatalysts and are still the most widely used electrocatalysts in low temperature polymer electrolyte membrane fuel cells (PEMFC) [11]. But a major drawback is the high cost of such electrocatalysts. Thus, extensive efforts have been paid to reduce the amount of the Pt electrocatalysts by increasing the utilization of Pt or via alloying with other metals [12–19]. Another rapidly emerging alternative is the development of new inexpensive non-Pt-based electrocatalysts with a comparable or even better electrocatalytic activity to that of Pt [2,3,20–28]. These include the use of Au nanoparticles-based cathodes [20,23–27], a combined use of Co-based complex together with manganese oxide [29–31], W_2C–Ag nanocrystalline composites [21] as well as bifunctional Ag–MnO_2 catalysts supported onto single-walled carbon nanotubes (SWNT) [22]. Au nanoparticles-based cathodes with controllable size and crystallographic orientation stand as more economically and cheap electrocatalysts for the ORR [25,27]. However, the contribution of the two-electron reduction pathway of O_2 to hydrogen peroxide is unavoidable. The produced hydrogen peroxide has a detrimental effect on the matrix of the polymer electrolyte membrane which separates the two parts of the fuel cell (i.e., the cathodic and the anodic sides) as well as on the overall performance of the fuel cell. A combined use of a second catalyst (i.e., manganese oxide nanoparticles) together with Au nanoparticles has been recently suggested as a novel strategy in the fabrication of efficient electrocatalysts towards

---

[*] Corresponding author. Tel.: +81 45 924 5404; fax: +81 45 924 5489.
E-mail addresses: msaada68@yahoo.com (M.S. El-Deab), ohsaka@echem.titech.ac.jp (T. Ohsaka).

[1] ISE Member.

[2] Permanent address: Department of Chemistry, Faculty of Science, Cairo University, Cairo, Egypt.

0013-4686/$ – see front matter © 2006 Elsevier Ltd. All rights reserved.
doi:10.1016/j.electacta.2006.08.041

the ORR [28]. This is based on the fact that manganese oxide has an excellent catalytic activity towards the chemical disproportionation of hydrogen peroxide into water and molecular oxygen [31]. This study aims at the investigation of the dependence of the electrocatalytic activity of the proposed binary catalyst on the loading level and the sequence of electrodeposition of both species. This was done to fabricate a cheap binary catalyst composed of the optimal amounts of both species quite sufficient to support effectively an apparent four-electron reduction of O_2 at reasonably low cathodic overpotential in replacement of the costly Pt-based electrocatalysts. Cyclic voltammetry (CV) as well as hydrodynamic voltammetry are employed to study the ORR in O_2-saturated 0.1 M KOH solution.

2. Experimental

Glassy carbon (GC) electrode and highly oriented pyrolytic graphite (HOPG) were used as the working electrodes. The GC electrodes were in the form of disks ($\phi = 3.0$ mm) sealed in a Teflon jacket having an exposed geometric surface area of 0.07 cm^2. Whereas, the HOPG electrodes were fabricated by freshly cleaving HOPG plates (supplied by NT-MDT Co., Russia) and then supporting them on a plastic substrate (the exposed geometric surface area is 0.15 cm^2). Cyclic voltammetric (CV) measurements were performed in a conventional two-compartment three-electrode Pyrex glass cell using a computer-controlled BAS 100 B/W electrochemical analyzer. A spiral Pt wire and an Ag/AgCl/KCl(sat.) (having an equilibrium potential of +197 mV versus standard hydrogen electrode (SHE)) were the counter and the reference electrodes, respectively. All potentials in this paper are reported against SHE. GC electrodes were mechanically polished first with no. 2000 emery paper, then with aqueous slurries of successively finer alumina powder (down to 0.06 μm) with the help of a polishing microcloth, and then sonicated for 10 min in Milli-Q water. Au nanoparticles were electrodeposited on the thus-prepared GC electrodes (nano-Au/GC) from 0.5 M Na_2SO_4 solution containing 1.0 mM Na[$AuCl_4$]. The Na_2SO_4 solution is used as the supporting electrolyte to avoid the possible chemical dissolution of the manganese oxide nanoparticles pre-deposited onto the GC (or HOPG) electrodes, although the electrodeposition of Au nanoparticles is usually carried out in strong acidic media (e.g., H_2SO_4) [32]. Fig. 1 shows a linear sweep voltammetry (LSV) for the electrodeposition of Au nanoparticles onto GC electrode ($d = 3.0$ mm) from neutral 0.5 M Na_2SO_4 solution containing 1.0 mM Na[$AuCl_4$] at a potential scan rate of 100 mV s^{-1}. This figure shows that the reduction peak of Au ions to elemental Au is centered at ca. + 0.7 V versus SHE. Thus, a potential step electrolysis from 1.1 to 0 V versus Ag/AgCl/KCl(sat.) was utilized to perform the electrodeposition of the Au nanoparticles from this neutral solution for different electrolysis time. Whereas, manganese oxide (MnOx) nanoparticles were electrodeposited onto the GC (or HOPG) electrodes with/without pre/post-electrodeposition of Au nanoparticles from a solution containing 0.1 M Na_2SO_4 + 0.1 M $Mn(CH_3COO)_2$ via cycling the potential between 0.0 and 0.4 V versus Ag/AgCl/KCl(sat.) at 20 mV s^{-1} for different number of potential cycles. Steady-state voltammograms were obtained at a GC disk ($\phi = 3.0$ mm)-Pt ring electrode (RRDE) using a rotary system from Nikko Keisoku (Japan) coupled with an ALS/chi 832A electrochemical analyzer bi-potentiostat (USA). The same procedure of the electrodeposition of the Au and/or MnOx nanoparticles has been performed for the GC disk of the RRDE as that employed for the GC electrode used for the CV measurements. The working electrode compartment was 200 cm^3 to eliminate any possible change of the O_2 concentration during the measurements. Prior to each experiment, O_2 gas was bubbled directly into the cell for 30 min to obtain an O_2-saturated 0.1 M KOH solution; during every measurement O_2 gas was flushed over the cell solution. The collection efficiency, *N*, of the RRDE was measured using 1.0 mM $K_3[Fe(CN)_6]$ in 0.5 M KCl, and a value of 0.38 ± 0.02 was obtained for the GC disk-Pt ring RRDE. All current densities were calculated on the basis of the geometric surface area of the electrodes (i.e., 0.07 cm^2). All the measurements were performed at room temperature (25 ± 1 °C). All chemicals used in this investigation were of analytical grade and were used without further purification. X-ray diffraction (XRD) measurements were performed on a Philips PW 1700 powder X-ray diffractometer, using Cu Kα_1 radiation ($\lambda = 1.54056$ Å) with a Ni filter working at 40 kV and 30 mA. Scanning electron microscopy (SEM) and electron diffraction spectroscopy (EDS) analysis of the Au (and/or MnOx) nanoparticles electrodeposited onto the GC electrodes was carried out using an JSM-T220 scanning electron microscope (JEOL Optical Laboratory, Japan) at an acceleration voltage of 20 kV and a working distance of 4–5 mm.

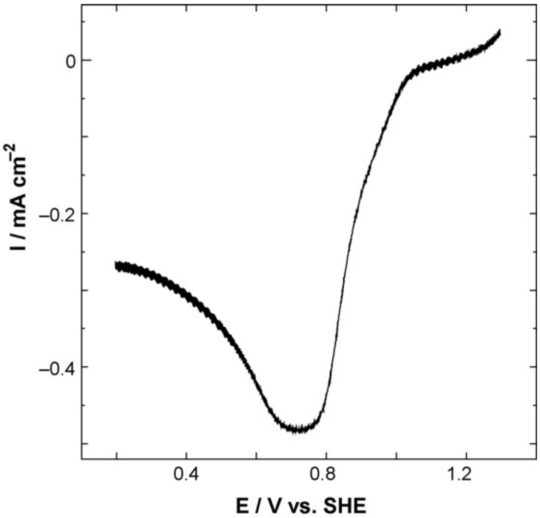

Fig. 1. LSV of Au nanoparticles electrodeposition at GC electrode ($f = 3.0$ mm) from 0.5 M Na_2SO_4 solution containing 1.0 mM Na[$AuCl_4$]. Potential scan rate: 100 mV s^{-1}.

3. Results and discussion

3.1. SEM, EDS and XRD characterization of the nano-MnOx and nano-Au electrodeposited onto HOPG and GC electrodes

Fig. 2a–d shows typical SEM images for HOPG electrodes loaded with (a) nano-Au, (b) nano-MnOx, (c) nano-Au/nano-

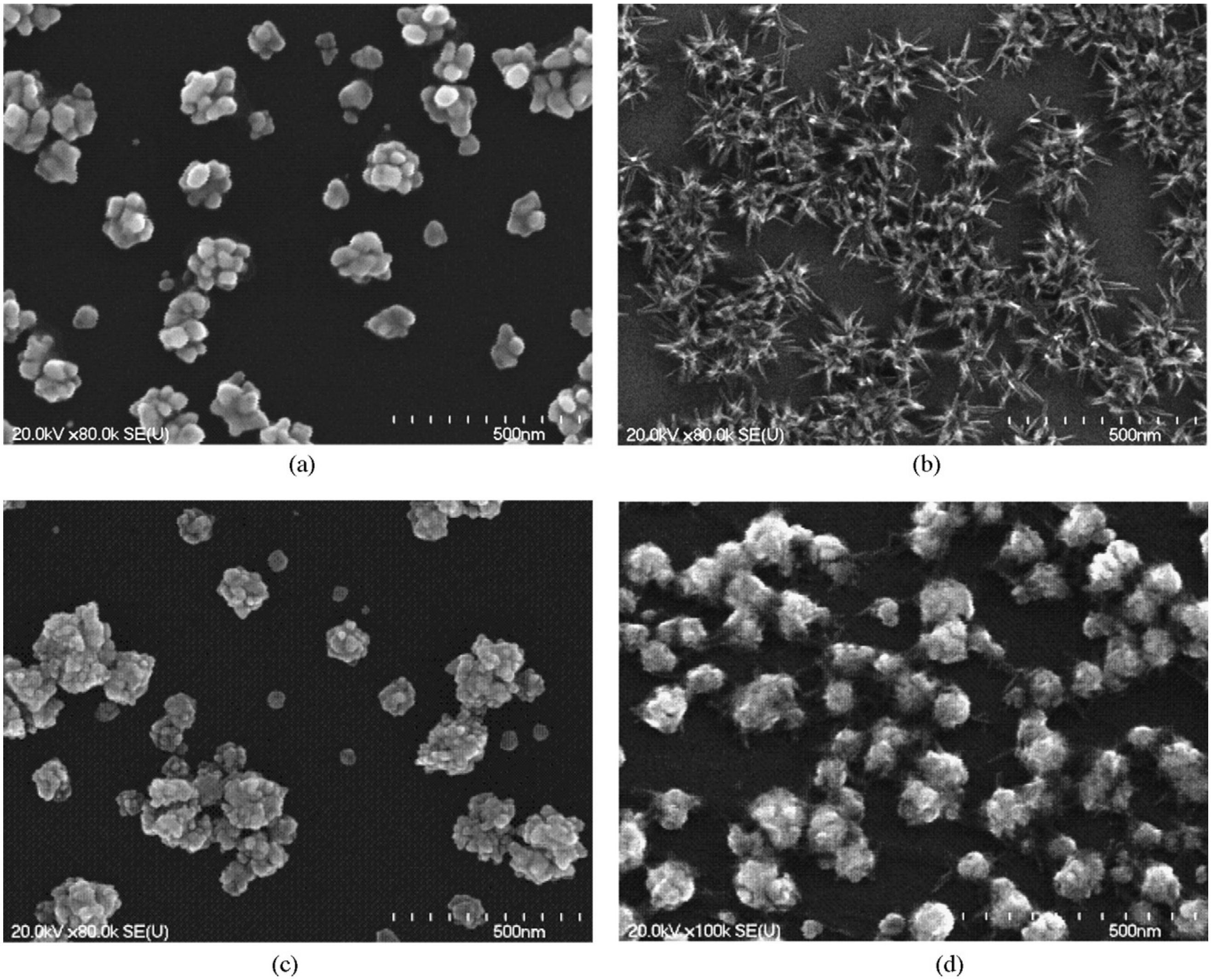

(a) (b) (c) (d)

Fig. 2. SEM images (at magnification factor of 80,000×) for the (a) nano-Au/HOPG, (b) nano-MnOx/HOPG, (c) nano-Au/nano-MnOx/HOPG and (d) nano-MnOx/nano-Au/HOPG electrodes. Au nanoparticles were electrodeposited for 300 s potential step from 1.1 to 0 V vs. Ag/AgCl/KCl(sat.) from 0.5 M Na_2SO_4 containing 1.0 mM $Na[AuCl_4]$. The electrodeposition of nano-MnOx was performed from 0.1 M Na_2SO_4 solution containing 0.1 M $Mn(CH_3COO)_2$ by applying 25 potential cycles between 0 and 0.4 V at 20 mV s^{-1}.

MnOx and (d) nano-MnOx/nano-Au. Electrodeposition of nano-MnOx and nano-Au was performed, respectively, by applying 25 potential cycles between 0 and 0.4 V vs. Ag/AgCl/KCl(sat.) in 0.1 M Na_2SO_4 + 0.1 M $Mn(Ac)_2$, and a potential step of 300 s from 1.1 to 0 V vs. Ag/AgCl/KCl(sat.) from the neutral bath of 0.5 M Na_2SO_4 solution containing 1.0 mM $Na[AuCl_4]$. Note that image c corresponds to the electrodeposition of nano-MnOx, firstly, onto the HOPG electrode followed by the electrodeposition of the Au nanoparticles, and vice versa for image d. Fig. 3a–g shows typical SEM images for GC electrodes loaded with (a) nano-Au, (b) nano-MnOx, (c and d) nano-Au/nano-MnOx and (e–g) nano-MnOx/nano-Au. Electrodeposition of nano-MnOx and nano-Au was performed, respectively, by applying (b–e) 25 and (f and g) 10 potential cycles between 0 and 0.4 V in 0.1 M Na_2SO_4 + 0.1 M $Mn(Ac)_2$, and (a, e and f) 300 s, (c) 60 s and (d and g) 180 s potential step from 1.1 to 0 V from the neutral bath of 0.5 M Na_2SO_4 solution containing 1.0 mM $Na[AuCl_4]$. Inspection of both figures (Figs. 2 and 3) shows some significant points:

1. The MnOx was electrodeposited in a porous nanorods texture onto the HOPG electrode (image b, Fig. 2) as well as onto the GC electrode (image b, Fig. 3) irrespective of the nature of the underlying substrate. This texture covers homogeneously the entire surface of the HOPG (and the GC) electrodes in a rather porous texture morphology, which enables the accessibility of the solution species to the underlying HOPG (or the GC) substrate through nano-channels across the MnOx nanotexture.
2. The morphology of the Au nanoparticles electrodeposited onto the bare HOPG and the GC electrodes from the neutral sodium sulfate solution is quite similar to those electrodeposited from the acidic H_2SO_4 solution [24,33]. See images marked ‘a’ in Figs. 2 and 3.

3. On the other hand, image d (Fig. 2) as well as images e–g (Fig. 3) shows the electrodeposition of MnOx nanorods onto the Au nanoparticles previously electrodeposited onto the HOPG and the GC electrodes, respectively. Consequently, the Au nanoparticles are partially covered with the MnOx.
4. The Au nanoparticles have been electrodeposited from the neutral Na_2SO_4 aqueous solution onto the nanotexture of the previously electrodeposited nano-MnOx without causing any damage of its nano-porous texture morphology (see images c and d of Fig. 3).

Fig. 4 shows the EDS spectra of GC electrodes loaded with different amounts of Au and MnOx nanoparticles. The peak intensities of both species vary with the extent and the sequence of their electrodeposition. Table 1 summarizes the relative atomic percent ratio of the Au and Mn versus the electrodeposition conditions. Inspection of this table reveals two points, i.e.: (i) the increase of the electrodeposition time of Au or the number of potential cycles employed for the MnOx electrodeposition increases each atomic percent and (ii) the electrodeposition of Au nanoparticles from the neutral bath does not wash up the pre-electrodeposited MnOx.

The highly crystalline nature of the HOPG substrate could, advantageously, enable the monitoring of the XRD pattern of each species (i.e., nano-Au and nano-MnOx). Fig. 5 shows The XRD patterns obtained at HOPG electrode loaded with (b) nano-Au, (c) nano-MnOx, (d) nano-Au/nano-MnOx and (e) nano-MnOx/nano-Au as compared with the bare HOPG electrode (curve a). The same electrodeposition conditions as in Fig. 2 are used. Inspection of this figure reflects some interesting features, i.e.:

1. The two peaks located at 2θ of about 26.4° and 54.8° correspond to the C(0 0 2) and C(0 0 4) basal planes of the HOPG substrate (see curves a–e).

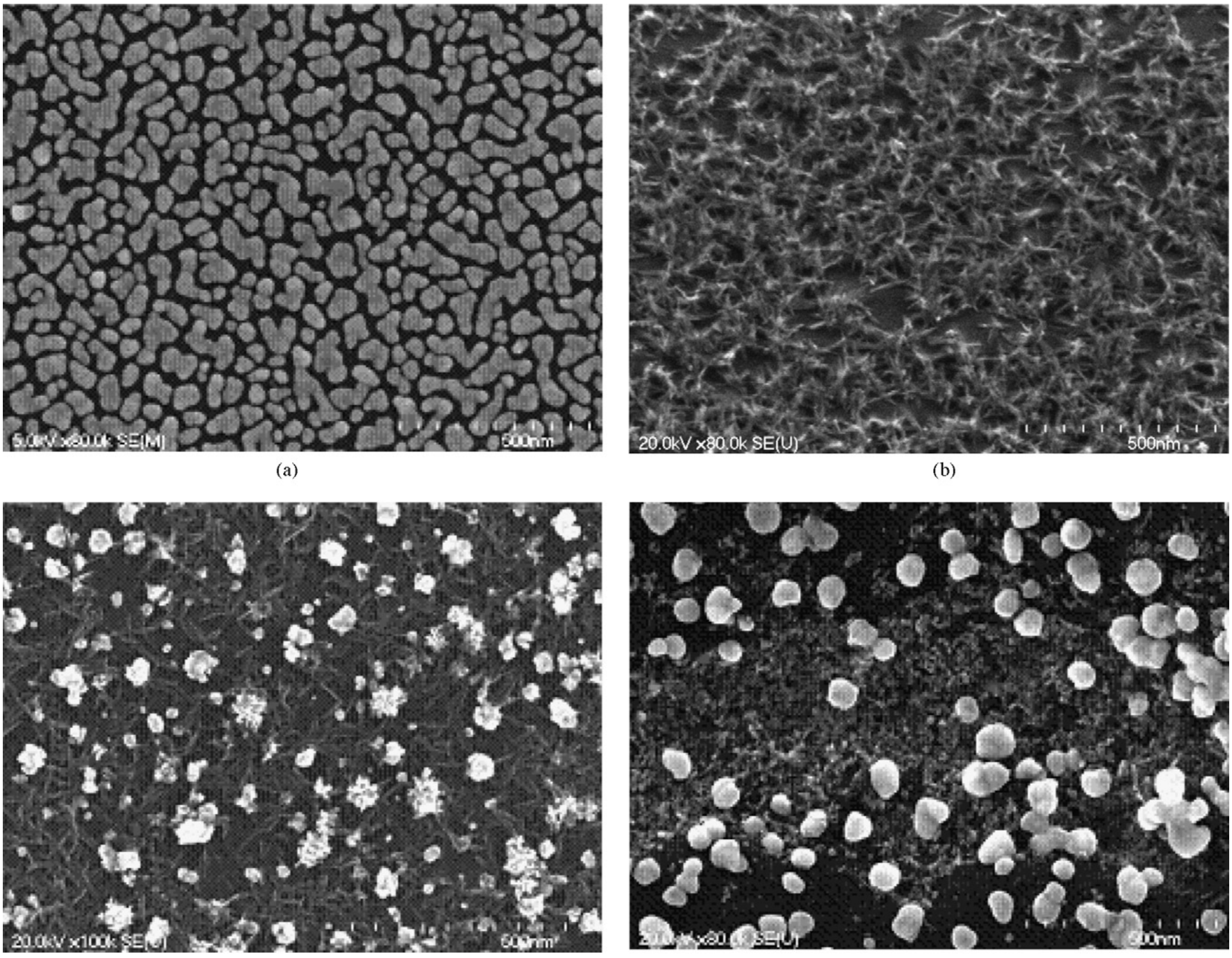

(a) (b)

(c) (d)

Fig. 3. SEM images (at magnification factor of 80,000×) for the (a) nano-Au/GC, (b) nano-MnOx/GC, (c and d) nano-Au/nano-MnOx/GC and (e–g) nano-MnOx/nano-Au/GC electrodes. Au nanoparticles were electrodeposited for (a, e, and f) 300 s, (c) 60 s and (d and g) 180 s potential step from 1.1 to 0 V vs. Ag/AgCl/KCl(sat.) from 0.5 M Na_2SO_4 containing 1.0 mM $Na[AuCl_4]$. The electrodeposition of nano-MnOx was performed from 0.1 M Na_2SO_4 solution containing 0.1 M $Mn(CH_3COO)_2$ by applying (b–e) 25 and (f and g) 10 potential cycles between 0 and 0.4 V at 20 mV s^{-1}.

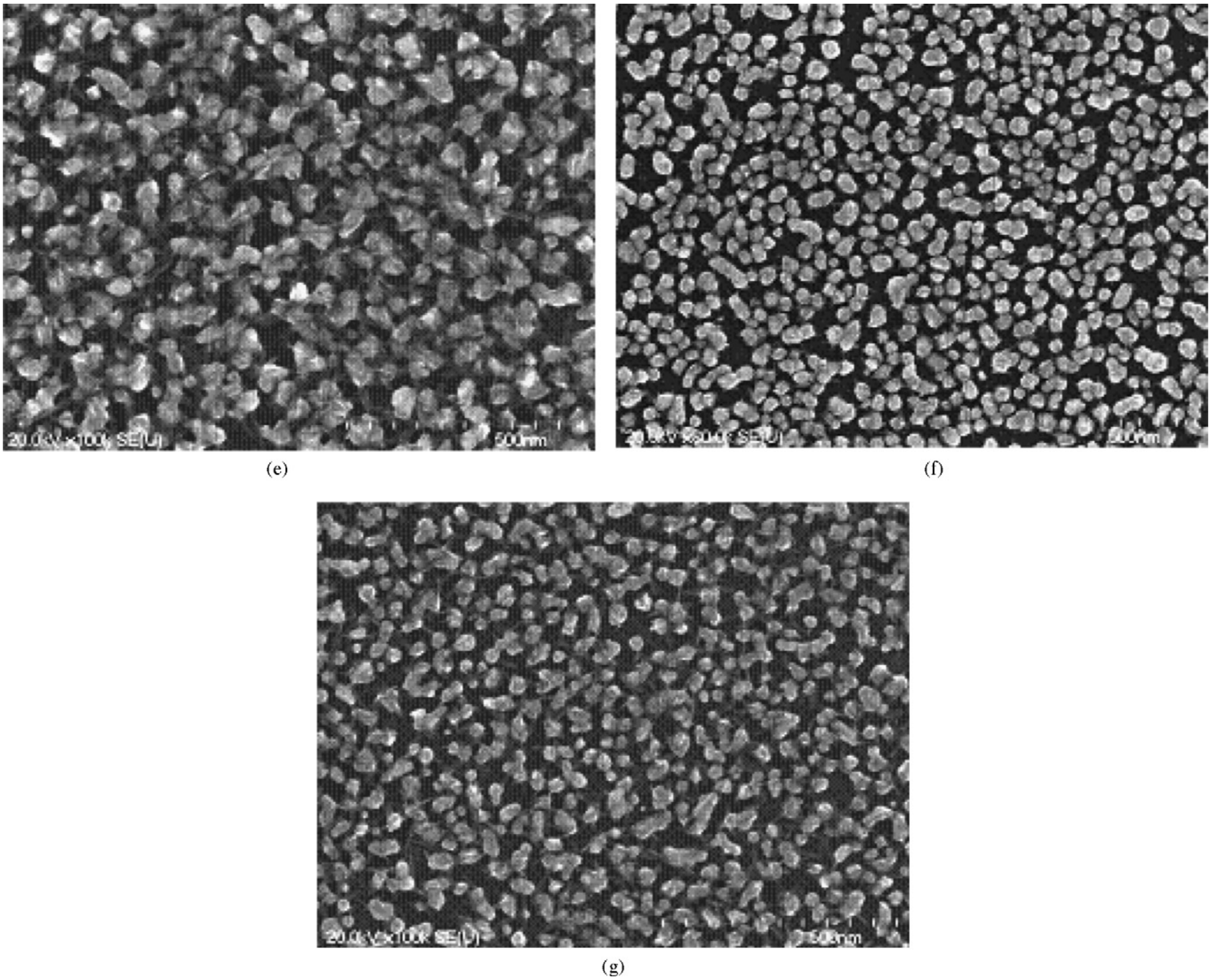

(e) (f) (g)

Fig. 3. (*Continued*).

Table 1
Variation of the atomic percent ratio of the nano-Au and nano-MnOx species as a function of the sequence and conditions of the electrodeposition of Au and MnOx nanoparticles onto the GC electrodes

Case	$t_{\text{nano-Au}}$[a]/s	$\text{NPC}_{\text{nano-MnOx}}$[b]	Au:MnOx[c]
a	60 (2)	25 (1)	9.45:7.75
b	300 (1)	25 (2)	19.75:11.95
c	300 (1)	10 (2)	18.85:6.10
d	180 (1)	10 (2)	11.90:7.85

The data were extracted from Fig. 4. The numbers within parentheses refer to the sequence of the electrodeposition. Thus, case a represents the electrodeposition of nano-MnOx, firstly, onto the bare GC electrode by applying 25 potential cycles followed by the electrodeposition of nano-Au (as a second step) for 60 s (corresponding to image c of Fig. 3).

[a] The width of the potential step employed for the electrodeposition of the Au nanoparticles onto the GC electrode (see Section 2).

[b] NPC is the number of potential cycles employed for the electrodeposition of the MnOx nanoparticles onto the GC electrode (see Section 2).

[c] The atomic percent as extracted from the EDS spectra (see Fig. 4).

2. The peaks located at 2θ values of about 38.5°, 44.4° and 64.6° correspond to the Au(1 1 1), Au(2 0 0) and Au(2 2 0) facets of the Au nanoparticles, respectively.
3. Interestingly, this figure shows that manganese oxide is electrodeposited in a crystalline phase as a sharp peak located at 2θ of ca. 26° emerged upon its electrodeposition (which is overlapped with the C(0 0 2) peak of the HOPG substrate. This peak can be clearly observed in curve e of this figure. This peak corresponds to the $(1\,1\,\bar{1})$ crystallographic plane of the manganite phase (manganese oxide hydroxide, MnOOH). The same phase of manganese oxide has been obtained upon the electrodeposition at Pt substrate [34].

3.2. *Evaluation of the electrocatalytic activity of the nano-MnOx/nano-Au/GC electrodes with different loadings towards the ORR*

3.2.1. *Variation of the nano-Au loading*

Fig. 6 shows CVs for the ORR obtained at (a) bare GC, (b) nano-MnOx/GC, (c–f) nano-Au/nano-MnOx/GC with different Au loadings, in O_2-saturated 0.1 M KOH. Curve g shows

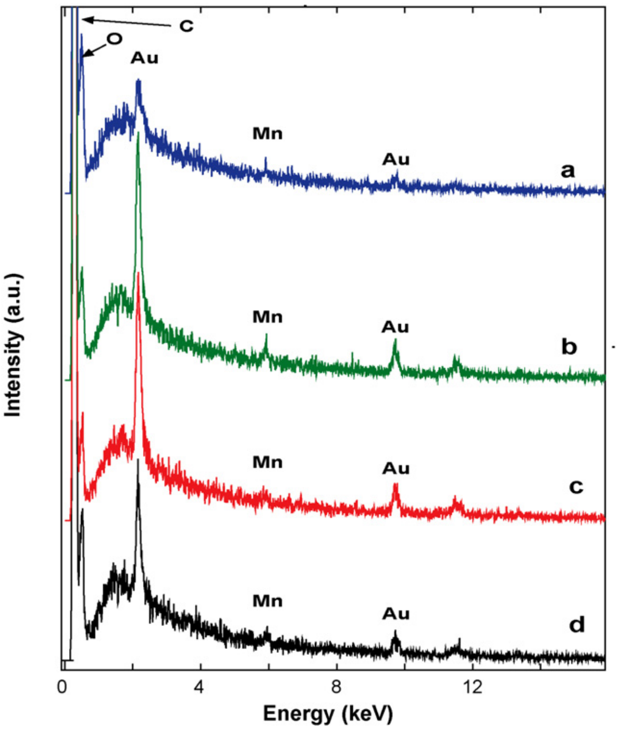

Fig. 4. (A) EDS spectra for the GC electrodes (analyzed area = 300 nm × 300 nm) loaded with different amounts of nano-Au and nano-MnOx. The EDS spectra shown as curves (a–d) of this figure correspond, respectively, to images (c, e–g) of Fig. 3.

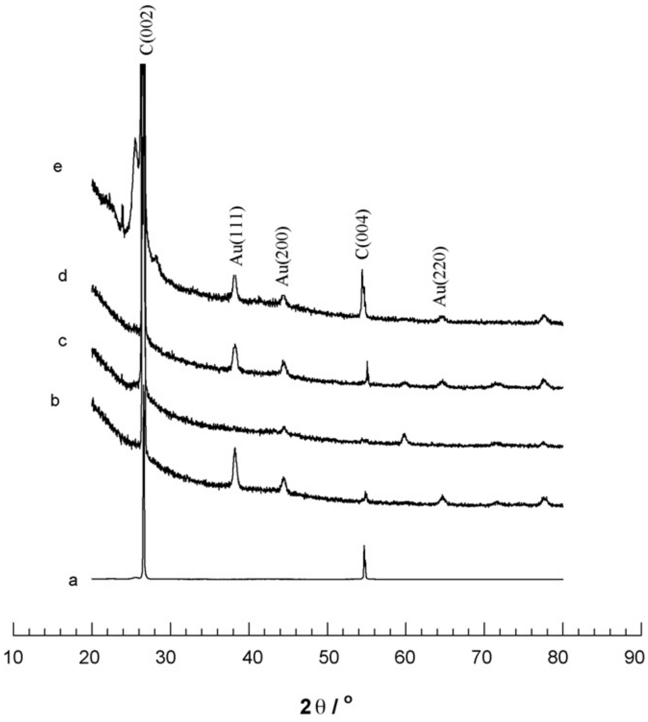

Fig. 5. XRD patterns for (a) bare HOPG, (b) nano-Au/HOPG, (c) nano-MnOx/HOPG, (d) nano-Au/nano-MnOx/HOPG and (e) nano-MnOx/nano-Au/HOPG electrodes. The electrodeposition conditions used for MnOx and Au nanoparticles were the same as in Fig. 2.

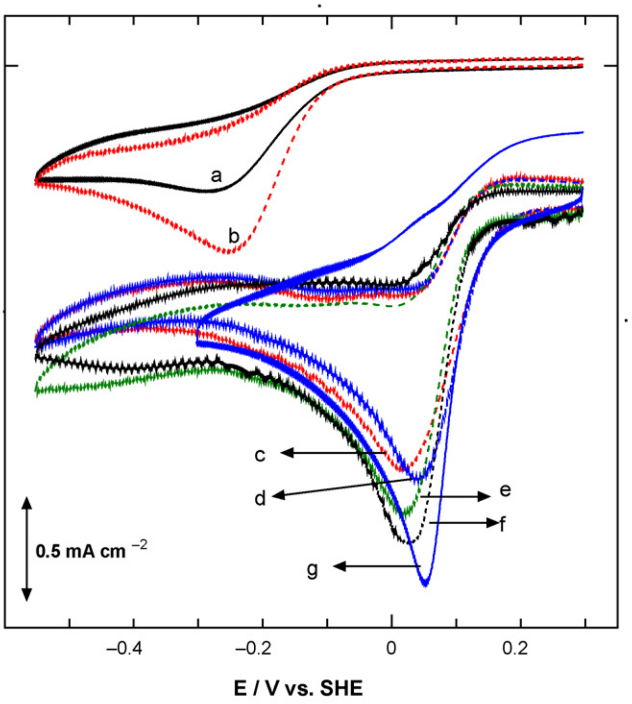

Fig. 6. CVs for the ORR in O_2-saturated 0.1 M KOH at (a) bare GC, (b) nano-MnOx/GC and (c–f) nano-Au/nano-MnOx/GC electrodes (f = 3.0 mm). SR = 100 mV s^{-1}. Electrodeposition of nano-MnOx was performed by applying 25 potential cycles between 0 and 0.4 V at 20 mV s^{-1} in an aqueous solution of 0.1 M Na_2SO_4 containing 0.1 M $Mn(CH_3COO)_2$. Au nanoparticles were electrodeposited onto the nano-MnOx/GC electrode by applying a potential step electrolysis from 1.1 to 0 V for (c) 60 s, (d) 120 s, (e) 180 s, and (f) 240 s from 0.5 M Na_2SO_4 solution containing 1.0 mM $Na[AuCl_4]$.

the CV for the ORR at the bare Pt electrode for comparison at which a direct four-electron reduction of oxygen to OH^- takes place exclusively. This figure shows that the electrodeposition of MnOx caused a significant increase of the peak current of the ORR without any significant shift of the peak potential. The increase of the peak current associated with the electrodeposition of the MnOx nanoparticles (curve b) is due to the catalytic disproportionation activity of nano-MnOx towards the electrogenerated hydrogen peroxide (HO_2^-) at the GC electrode in alkaline medium, which can be represented as

$$O_2 + H_2O\ +\ 2e^- \rightarrow\ HO_2^- + OH^- \qquad (1)$$

$$HO_2^- \xrightarrow{\text{nano-MnOx}} \tfrac{1}{2}O_2 + OH^- \qquad (2)$$

While the different loading of Au caused a pronounced shift of the oxygen reduction peak potential to the positive direction of potential. In fact, this shift in the peak potential indicates the predominance of the ORR at the electrodeposited Au nanoparticles rather than at the bare portion of the GC electrode. Electrodes marked e and f showed the highest peak current among the examined electrodes being comparable to that of the Pt electrode (curve g).

Fig. 7 shows the RRDE voltammograms for the ORR obtained at the (a) bare GC, (b) nano-MnOx/GC and (c–f) nano-Au/nano-MnOx/GC disk electrodes (f = 3.0 mm) in O_2-saturated

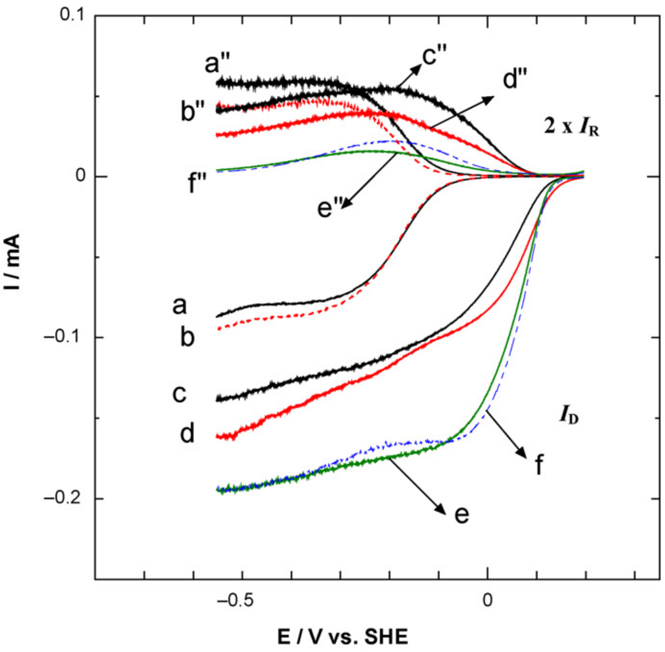

Fig. 7. RRDE voltammograms for the ORR, in O_2-saturated 0.1 M KOH, at (a) bare GC, (b) nano-MnOx/GC, (c–f) nano-Au/nano-MnOx/GC disk electrodes (f = 3.0 mm). Rotation rate: 400 rpm. Potential scan rate of the disk electrode: 10 mV s^{-1}. Curves (a″–f″) represent the corresponding Pt-ring current (polarized at +0.5 V). Electrodeposition of MnOx and Au nanoparticles was performed as described in Fig. 6.

0.1 M KOH. Note that the nano-MnOx was, firstly, electrodeposited onto the GC electrode via 25 potential cycles between 0 and 0.4 V at 20 mV s^{-1}, then followed by the electrodeposition of nano-Au onto the nano-MnOx/GC electrode via (c) 60 s, (d) 120 s, (e) 180 s and (f) 240 s potential step from 1.1 to 0 V. The Pt ring electrode was potentiostated at +0.5 V and the measured ring currents (which represent the oxidation of the hydrogen peroxide electrogenerated at the relevant disk electrode) are shown in the upper side of the graph (a″–f″). This figure shows that the electrodeposition of minute amount of Au nanoparticles (curve c) causes a significant positive shift of the onset of the ORR along with an increase of the disk current compared to the bare GC disk electrode (curve a). Further prolonged electrodeposition of Au nanoparticles leads to more pronounced positive shift of the onset potential of the ORR along with a noticeable increase of the disk current. Note that curve f (corresponding to 240 s deposition time of Au) does not show any pronounced improvement in disk current or in the onset potential of the ORR current flow as compared to curve e (180 s). But a slight increase of the corresponding ring current is observed (curve f″).

3.2.2. Variation of the nano-MnOx loading

Fig. 8 shows the CVs for the ORR obtained at (a) bare GC, (b) nano-Au/GC and (c–e) nano-MnOx/nano-Au/GC electrodes with different loadings of nano-MnOx in O_2-saturated 0.1 M KOH. MnOx loading was carried out for (c) 2, (d) 10 and (e) 25 potential cycles. This figure shows an observable enhancement of the ORR in terms of peak potential and current upon the loading of Au nanoparticles (curve b). While a rather broad peak for the ORR was observed in the more negative potential region upon the loading of nano-MnOx onto the nano-Au/GC electrodes (curves c–e). This might be due to the partial deactivation of the pre-deposited Au nanoparticles by the nano-MnOx (see images e-g in Fig. 3). In comparison to the bare GC electrode (curve a), the peak potential of the ORR at those electrodes (curves c–e) is more positive and also its peak current intensity is higher. The corresponding steady-state hydrodynamic voltammograms for the ORR are shown in Fig. 9 in which they were obtained at (a) bare GC, (b) nano-Au/GC and (c–e) nano-MnOx/nano-Au/GC disk electrodes (f = 3.0 mm) in O_2-saturated 0.1 M KOH. Note that the nano-MnOx was electrodeposited onto the nano-Au/GC electrode via (c) 2, (d) 10 and (e) 25 potential cycles. The corresponding Pt ring currents are shown in the upper side of the graph (curves a″–e″). This figure shows that the nano-Au/GC disk electrode (curve b) supports the highest current for the ORR associated with low value of the corresponding ring current (see curve b″) at fairly low cathodic polarization (at about 0 V versus SHE). This disk current maximum diminishes at higher cathodic potentials and a significant increase of the ring current starts to emerge. This behaviour is similar to that obtained at the Au(1 0 0)-rich Au nanoparticles-electrodeposited GC disk electrode [27], indicat-

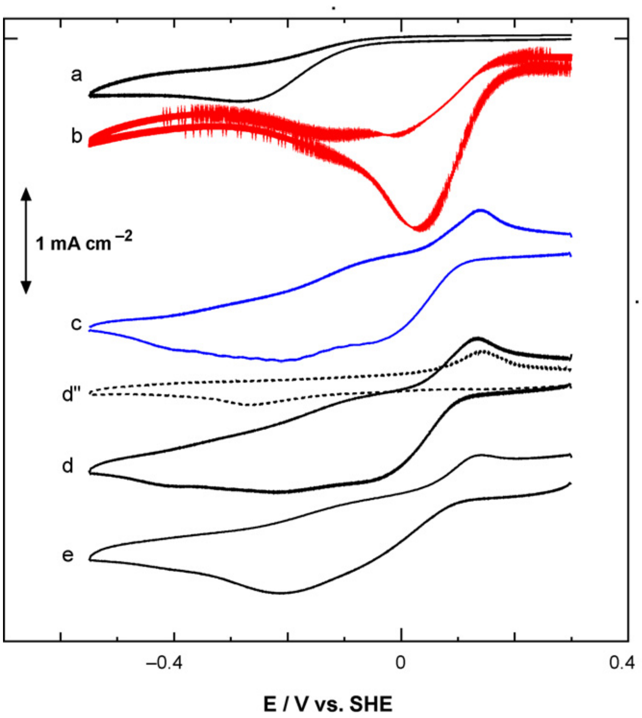

Fig. 8. CVs for the ORR in O_2-saturated 0.1 M KOH at (a) bare GC, (b) nano-Au/GC and (c–e) nano-MnOx/nano-Au/GC electrodes (f = 3.0 mm). SR = 100 mV s^{-1}. Au nanoparticles were electrodeposited onto the GC electrode by applying a 300 s potential step electrolysis from 1.1 to 0 V from 0.5 M Na_2SO_4 solution containing 1.0 mM Na[$AuCl_4$]. Electrodeposition of nano-MnOx onto the nano-Au/GC electrode was performed by applying (c) 2, (d) 10 and (e) 25 potential cycles between 0 and 0.4 V at 20 mV s^{-1} in an aqueous solution of 0.1 M Na_2SO_4 containing 0.1 M $Mn(CH_3COO)_2$. Curve d″ represents the blank CV response of the same electrode of curve d in N_2-saturated 0.1 M KOH solution at a potential scan rate of 100 mV s^{-1}.

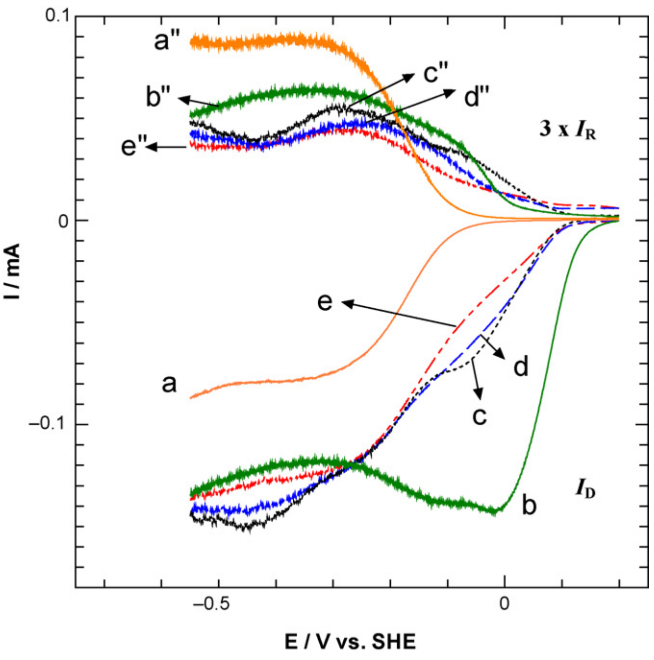

Fig. 9. RRDE voltammograms for the ORR, in O_2-saturated 0.1 M KOH, at (a) bare GC, (b) nano-Au/GC and (c–e) nano-MnOx/nano-Au/GC disk electrodes (f = 3.0 mm). Rotation rate: 400 rpm. Potential scan rate of the disk electrode: 10 mV s^{-1}. Curves (a″–e″) represent the corresponding Pt-ring current (polarized at +0.5 V). Electrodeposition of MnOx and Au nanoparticles was performed as described in Fig. 8.

ing that this nano-Au/GC electrode (curve b) is enriched in the Au(1 0 0) orientation. However, the electrodeposition of nano-MnOx (albeit at low loadings, case c) was found to weaken such a unique characteristic of the nano-Au/GC itself. This might originate from the fact that the electrodeposition of MnOx takes place at the previously deposited Au nanoparticles (see, for example, image d of Fig. 2 and images e–g of Fig. 3).

3.3. Estimation of the fraction of the electrogenerated H_2O_2 at the nano-MnOx/nano-Au/GC electrodes with different loadings

The percentage of the electrogenerated hydrogen peroxide ($X_{H_2O_2}$) during the ORR can be estimated using the following equation [12]:

$$X_{H_2O_2} = \frac{2I_R/N}{I_D + (I_R/N)} \times 100 \tag{3}$$

where I_R is the ring current, I_D the disk current and N is the collection efficiency of the RRDE electrode. Thus, $X_{H_2O_2} = 0$ if $I_R = 0$, i.e., exclusive four-electron reduction of O_2 to water, while this value is 100% if I_D equals (I_R/N). Fig. 10A shows the variation of $X_{H_2O_2}$ as a function of the amount of the electrodeposited Au nanoparticles onto the nano-MnOx/GC disk electrode (the data were extracted from Fig. 7). This figure shows that the GC electrode supports an exclusive two-electron reduction of O_2 to H_2O_2 as the value of $X_{H_2O_2}$ is very close to 100%. On the other hand, electrodeposition of nano-MnOx onto the GC disk electrode caused a noticeable lowering of the $X_{H_2O_2}$ value down to ca. 80% (curve b) due to the catalytic disproportionation activity of nano-MnOx towards H_2O_2 (see Eq. (2) above). Furthermore, the electrodeposition of minute amount of Au nanoparticles caused a further significant lowering of the $X_{H_2O_2}$ value (curve c). More increase of the amount of the electrodeposited Au nanoparticles resulted in a more pronounced decrease in $X_{H_2O_2}$ until a certain loading of Au (180 s, curve e) beyond which a slight increase of this value was observed (see curve f). This means a partial loss of the synergistic enhancing effect of Au and MnOx nanoparticles on the ORR. That is, the electrodeposition of the excess Au nanoparticles onto the bare portion of the GC substrate, which is covered with insulating

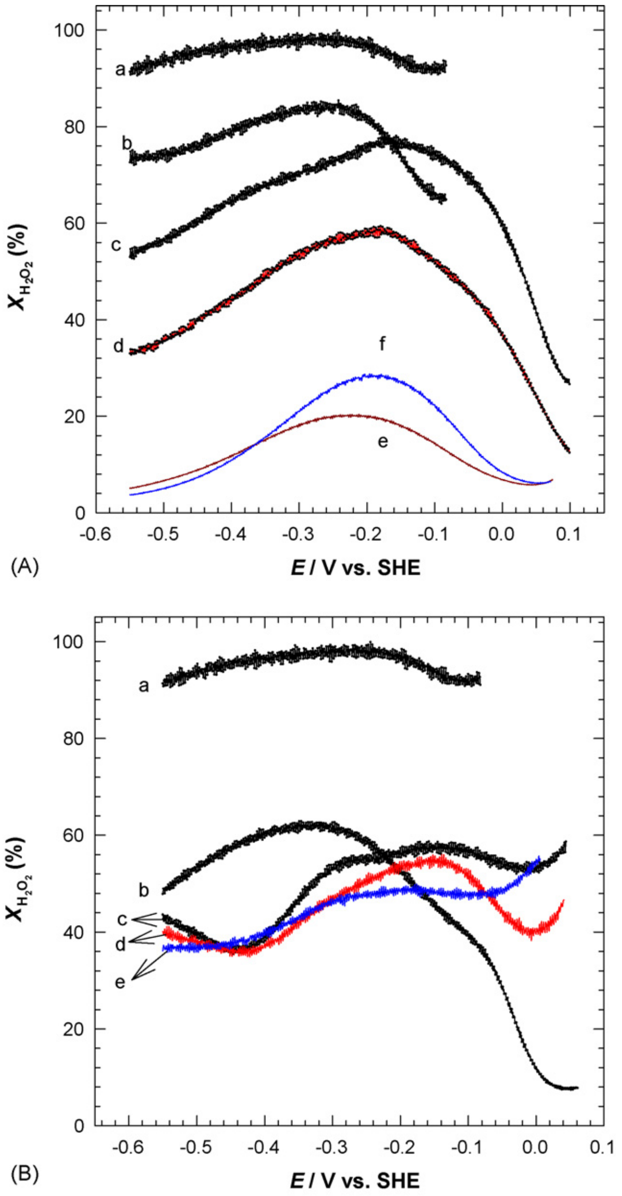

Fig. 10. (A) Variation of the percent of the electrogenerated H_2O_2 ($X_{H_2O_2}$) as a function of the extent of the Au nanoparticles loadings onto the nano-MnOx/GC electrode. Same notation as in Fig. 7 is used. (B) Variation of the percent of the electrogenerated H_2O_2 ($X_{H_2O_2}$) as a function of the extent of the MnOx nanoparticles loadings onto the nano-Au/GC electrode. Same notation as in Fig. 9 is used.

nano-MnOx fibrous texture, results in a decrease in the active area of the nano-MnOx available for the catalytic disproportionation of the hydrogen peroxide electrogenerated on the Au nanoparticles. Fig. 10B shows the variation of $X_{H_2O_2}$ as a function of the amount of the electrodeposited MnOx nanoparticles onto the nano-Au/GC disk electrode (the data were extracted from Fig. 9). This figure shows that the electrodeposition of Au nanoparticles onto the bare GC disk electrode support an almost four-electron reduction pathway of O_2 to water at relatively positive potential (at ca. 0 V versus SHE) as can be seen from the low fraction of the electrogenerated H_2O_2 (<10%). This fraction increases as the disk electrode potential is swept to more negative values and it reaches a maximum value of ca. 60% at ca. −0.3 V. The electrodeposition of nano-MnOx, even though at low loading (curve c), caused a significant increase of $X_{H_2O_2}$ at relatively positive potential (ca. −0.2 V) compared to that obtained at the GC electrode loaded with the Au nanoparticles alone (curve b). But this electrode supports lower values of $X_{H_2O_2}$ at more negative potentials than ca. −0.3 V. The large values of $X_{H_2O_2}$ obtained at the nano-MnOx/nano-Au/GC disk electrodes at the relatively positive potential indicate the electrodeposition of the nano-MnOx onto the nano-Au. This in turn leads to the observed de-activation of the nano-Au/GC electrode towards an efficient four-electron reduction of O_2.

4. Conclusions

The electrocatalytic activity of Au and MnOx nanoparticles binary electrocatalysts electrodeposited onto GC substrates has been examined towards the oxygen reduction in alkaline medium as a function of the loading extent and sequence of electrodeposition of both species. This was done aiming at the fabrication of a binary catalyst electrode composed of the optimum amounts of both species while having the highest possible electrocatalytic activity towards the electrocatalytic reduction of O_2 to hydrogen peroxide through two-electron reduction at the nano-Au followed by chemical decomposition of the electrogenerated hydrogen peroxide to water and molecular oxygen at the nano-MnOx. This bifunctional mechanism leads ultimately to an apparent four-electron reduction of oxygen. The electrode prepared by the electrodeposition of nano-MnOx (25 potential cycles) followed by the Au nanoparticles electrodeposition (for 180 s) showed the best performance towards an apparent four-electron reduction of O_2. Excessive electrodeposition of Au nanoparticles (more than 180 s) is thought to decrease the active area of the nano-MnOx accessible to hydrogen peroxide and thus, leading to a partial loss of its catalytic disproportionation activity towards hydrogen peroxide. Inversing the order of the electrodeposition of both species resulted in a totally different undesired behaviour of the electrode.

Acknowledgements

This work was financially supported by Grant-in-Aids for Scientific Research (nos. 12875164 and 14050038) and “Scientific Research (A)” (no. 10305064) from the Ministry of Education, Culture, Sports, Science and Technology, Japan and also by New Energy and Industrial Technology Development Organization (NEDO), Japan. The authors thank Dr. A. Genseki, and T. Kiguchi at Center for Advanced Materials Analysis of Tokyo Institute of Technology for their support in the SEM, EDS and XRD measurements of the electrodeposited nanoparticles of Au and MnOx.

References

[1] K. Kinoshita, Electrochemical Oxygen Technology, Wiley, 1992.
[2] T. Ohsaka, M.S. El-Deab, Recent Research Developments in Electrochemistry, vol. 7, Transworld Research Network Publisher, India, 2004 (and the references cited therein).
[3] B. Wang, J. Power Sources 152 (2005) 1 (and the references cited therein).
[4] N. Wakabayashi, M. Takeichi, H. Uchida, M. Watanabe, J. Phys. Chem. B 109 (2005) 5836.
[5] C.C. Yang, Int. J. Hydrogen Energy 29 (2004) 135.
[6] J.S. Park, C.O. Park, H.J. Kim, N. Miura, Solid State Ionics 176 (2005) 1371.
[7] J.L. Fernandez, D.A. Walsh, A.J. Bard, J. Am. Chem. Soc. 127 (2005) 357.
[8] H. Kaneko, T. Okamura, H. Taimatsu, Y. Matsuki, H. Nishida, Sens. Actuators B 108 (2005) 331.
[9] J.S. Yang, J.J. Xu, Electrochem. Commun. 5 (2003) 306.
[10] H. Huang, W.K. Zhang, M.C. Li, Y.P. Gan, J.H. Chen, Y.F. Kuang, J. Colloid Interface Sci. 284 (2005) 593.
[11] S. Gottesfeld, T.A. Zawodzinski, in: R.C. Alkire, H. Gerischer, D.M. Kolb, C.W. Tobias (Eds.), Advances in Electrochemical Science and Engineering, vol. 5, Wiley-VCH, Weinheim, 1997 (Chapter 4).
[12] U.A. Paulus, T.J. Schmidt, H.A. Gasteiger, R.J. Behm, J. Electroanal. Chem. 495 (2001) 134.
[13] U.A. Paulus, A. Wokaun, G.G. Scherer, T.J. Schmidt, V. Stamenkovic, V. Radmilovic, N.M. Markovic, P.N. Ross, J. Phys. Chem. B 106 (2002) 4181.
[14] E. Antolini, J.R.C. Salgado, L.G.R.A. Santos, G. Garcia, E.A. Ticianelli, E. Pastor, E.R. Gonzalez, J. Appl. Electrochem. 36 (2006) 355.
[15] J.-F. Drillet, A. Ee, J. Friedemann, R. Kotz, B. Schnyder, V.M. Schmidt, Electrochim. Acta 47 (2002) 1983.
[16] E. Higuchi, H. Uchida, M. Watanabe, J. Electroanal. Chem. 583 (2005) 69.
[17] M.-K. Min, J. Cho, K. Cho, H. Kim, Electrochim. Acta 45 (2000) 4211.
[18] A.B. Anderson, J. Roques, S. Mukerjee, V.S. Murthi, N.M. Markovic, V. Stamenkovic, J. Phys. Chem. B 109 (2005) 1198.
[19] N.M. Markovic, H.A. Gasteiger, P.N. Ross, J. Phys. Chem. B 100 (1996) 6715.
[20] J. Hernandez, J. Solla-Gullon, E. Herrero, J. Electroanal. Chem. 574 (2004) 185.
[21] H. Meng, P.K. Shen, Electrochem. Commun. 8 (2006) 588.
[22] F.-P. Hu, X.-G. Zhang, F. Xiao, J.-L. Zhang, Carbon 43 (2005) 2931.
[23] M.S. El-Deab, T. Ohsaka, Electrochim. Acta 47 (2002) 4255.
[24] M.S. El-Deab, T. Okajima, T. Ohsaka, J. Electrochem. Soc. 150 (2003) A851.
[25] M.S. El-Deab, T. Sotomura, T. Ohsaka, J. Electrochem. Soc. 152 (2005) C1.
[26] F. Gao, M.S. El-Deab, T. Okajima, T. Ohsaka, J. Electrochem. Soc. 152 (2005) A1226.
[27] M.S. El-Deab, T. Sotomura, T. Ohsaka, Electrochem. Commun. 7 (2005) 29.
[28] M.S. El-Deab, T. Ohsaka, J. Electrochem. Soc. 153 (2006) A1365.
[29] L. Mao, K. Arihara, T. Sotomura, T. Ohsaka, Electrochim. Acta 49 (2004) 2515.
[30] K. Arihara, L. Mao, P.A. Liddell, E. Marina-Ochoa, A.L. Moore, T. Imase, D. Zhang, T. Sotomura, T. Ohsaka, J. Electrochem. Soc. 151 (2004) A2047.
[31] L. Mao, T. Sotomura, K. Nakatsu, N. Koshiba, D. Zhang, T. Ohsaka, J. Electrochem. Soc. 149 (2002) A504.
[32] M.O. Finot, M.T. McDermont, J. Electroanal. Chem. 488 (2000) 125.
[33] M.S. El-Deab, T. Sotomura, T. Ohsaka, J. Electrochem. Soc. 152 (2005) C730.
[34] M.S. El-Deab, T. Ohsaka, Angew. Chem. Int. Ed. 45 (2006) 5963.